Quartz under stress: Raman calibration and applications to geobarometry of metamorphic inclusions

Bruno Reynard[1], Xin Zhong[2]

[1]Laboratoire de Géologie de Lyon, Univ Lyon, ENS de Lyon, Univ Lyon1, CNRS, France
5   [2]Institute of Geological Sciences, Freie Universität Berlin, 12249 Berlin, Germany

Correspondence to: Bruno Reynard (bruno.reynard@ens-lyon.fr)

Abstract. An experimental calibration of the three major Raman peaks of quartz with hydrostatic pressure and uniaxial differential stress is presented, and implications for their use in geobarometry based on Raman spectroscopy of quartz inclusions is discussed. The position of 206 cm^{-1} peak depends only on hydrostatic pressure P, and its pressure dependence

10   is recalibrated with a peak fitting procedure that is more adequate for Raman barometry than previous calibrations. The position of the 128 and 464 cm^{-1} peaks depends on P and also on differential stress σ, which can be determined from the position of these two peaks knowing hydrostatic pressure from the position of the 206 cm^{-1} peak. The results obtained here are different from those inferred previously from first-principles calculations. The present calibration provides direct relationships between Raman shifts and stress, with a simple formulation of residual pressure and differential stress

15   assuming uniaxial stress along the *c*-axis of quartz inclusions. It is tested on data from experimental and natural inclusions. Residual pressures from the present calibration are similar within uncertainties to those obtained with previous experimental calibration within uncertainties, and experimental inclusions yield residual pressures consistent with synthesis pressure. Inconsistent residual differential stresses are obtained from the 128 and 464 cm^{-1} peaks on some experimental inclusions, providing a criterion for identifying inclusions under complex stress conditions that are not appropriate for geobarometry.

20   Recent data on natural inclusions show self-consistent differential stress, consistent with the assumption of major stress along symmetry axis of the inclusion crystals and with values expected from elastic models. The average pressure values from the 128 and 464 cm^{-1} peaks is similar to the residual pressure from the 206 cm^{-1} peak that depends only on hydrostatic pressure. It can be used to obtain pressure when the 206 cm^{-1} peak position cannot be used due to interference with host mineral peaks. Using the 128 and 464 cm^{-1} peaks alone, or averaging either 128 and 206 or 206 and 464 cm^{-1} peaks can

25   induce systematic bias in the residual pressure determination. Applications of the present results to natural inclusions suggest that combined determination of residual pressure and differential stress may be used both for barometry and thermometry pending further calibration.

1 Introduction

30 Raman spectroscopy has been used over two decades for determining residual pressures in mineral inclusions in diamonds (Izreali et al., 1999) and metamorphic minerals, principally garnets (Enami et al., 2007; Parkinson and Katayama, 1999). Entrapment pressures calculated from thermo-elastic modeling provide a determination of metamorphic pressures (Angel et al., 2017b; Kohn, 2014; Zhong et al., 2019) that is independent of those obtained from metamorphic phase equilibria through thermodynamic modeling (Connolly, 1990; Holland and Powell, 1998). The method has been validated with experimental

35 entrapment of quartz in garnet at controlled hydrostatic pressures (Bonazzi et al., 2019; Thomas and Spear, 2018).

Quartz is often used because it is a common mineral of nearly pure chemistry, hence the position of its Raman peaks depends on intensive parameters and not chemical variations. Accurate determinations of residual pressures rely among others on precise determinations of the Raman peak shifts with pressure that are provided by diamond anvil cell (DAC) experiments (Schmidt and Ziemann, 2000). Differential stresses also influence the calculations of residual pressures, and

40 determinations of strains from Raman frequency of quartz inclusions have relied on first-principles calculations of Raman peak shifts (Murri et al., 2019), a method that was also successfully used for determining differential stresses in high-pressure experiments (Reynard et al., 2019), but that is backed only by experimental data at liquid helium temperature (Briggs and Ramdas, 1977; Tekippe et al., 1973).

New experiments were performed to determine the Raman peak shifts induced by hydrostatic and non-hydrostatic stresses.

45 Consequences for barometric applications are discussed based on available data on artificial inclusions from piston-cylinder experiments (Bonazzi et al., 2019), and on recent datasets on natural quartz inclusions in different suites of metamorphic rocks (Cisneros et al., 2021; Gonzalez et al., 2019; Zhong et al., 2019).

2 Experiments

Raman spectra were obtained with a Horiba™ HR Evolution using a 532.31 nm excitation from DPSS laser and 1800 gr/mm

50 at LGL in ENS de Lyon. Only the three most intense Raman peaks at 128, 206 and 464 cm^{-1} are analyzed, and will be referred to by these numbers in the reminder of the text. A series of experiments were first performed with calibration against silicon standard. In order to check for instrumental drift, sharp Hg 18312.55 or He 18516.59 cm^{-1} lines were recorded along with spectra in a second series of experiments (Fig. 1). Maximum drift of the reference lines position during one experimental session is 0.5 cm^{-1} and was systematically corrected. The measured separation between the two reference

55 lines is in average of 204.03 cm^{-1} with a maximum deviation of 0.15 cm^{-1}. The TO-LO splitting of the 128 cm^{-1} peak was determined by varying a polarizer orientation to enhance one component with respect to the other (Fig. 1). Quartz inclusions in eclogitic garnets from the Bergen Arc (Zhong et al., 2019) were studied in Freie Universität Berlin. Raman spectra were obtained with a Horiba ISA Dilor Labram confocal Raman spectrometer using the 532 nm line of a Nd:YAG, 1800 gr/mm gratings, and Olympus 50× and 100× objectives. The laser energy was set at ca. 10 mW. Typical duration for each

60 measurement was 1 to 2 min with >5 times repetition to obtain good signal to noise ratio. Immediately after each inclusion

measurement, a gem-quality quartz crystal was measured as stress-free reference material to obtain the wavenumber shift of quartz inclusions due to residual stress.

Peak positions were fitted using symmetric Voigt profiles although some bands, in particular the 206 cm^{-1} peak, are slightly asymmetrical in shape. This ensures the present calibration is comparable with data obtained on natural inclusions where

65 Voigt profile must be used because interference with band of the host garnet do not allow to use more complex function to fit peak positions. Nominal frequencies of the three main quartz peaks of 127.1(2), 206.1(2) and 464.2(2) are obtained from internally calibrated spectra (Fig. 1). For the sake of comparison with previous studies (Bonazzi et al., 2019; Schmidt and Ziemann, 2000; Cisneros et al., 2021; Gonzalez et al., 2019; Zhong et al., 2019), all data were normalized to match ambient condition values of 128, 206, and 464 cm^{-1}.

70 Raman spectra of quartz were measured under hydrostatic pressure on randomly oriented small crystals (<10 µm) in a DAC in a hydrostatic methanol-ethanol-water mixture (Reynard et al., 2015; Reynard et al., 2019). Pressure was measured with ruby fluorescence (Piermarini et al., 1975) for comparison with previous data (Schmidt and Ziemann, 2000). A Deben™ 5kN compression cell was used to compress at ambient temperature under uniaxial force parallelepipeds of quartz that were cut along or perpendicular to the *c*-axis, in a similar fashion to former experiments at 4 K (Tekippe et al., 1973). Orientation

75 was performed optically with respect to crystalline faces with an estimated accuracy of 3°. The applied force is converted to stress by dividing with the cross section of the crystal rod, which was measured with an estimated uncertainty of 2%. A supplementary data sheet provides results from successful experiments and an example of failed experiment with early rupture of the crystal.

3. Elastic modeling

80 Interpretation of the Raman data on quartz inclusions relies on modeling of the residual pressure and stress for a given host, generally garnet. The unit cell parameters of quartz are fitted based on the X-ray data measured at ambient pressure high temperature (Carpenter et al., 1998), and at ambient temperature high pressure (Angel et al., 1997) with an EoS taking into account a curved alpha-beta transition (Angel et al., 2017a). The fitted EoS allows extrapolation to high P-T conditions. The residual stresses are calculated based on an analytical solution (Zhong et al., 2021) assuming a pure almandine garnet host.

85 The model involves extrapolation of the EoS to high pressure and temperature. Spherical inclusion entrapped in infinite, isotropic host is assumed. Entrapment stress is assumed to be hydrostatic. The model considers the elastic anisotropy of the inclusion. Compressive stress is defined as negative.

Results show that expected residual pressures are generally positive for most crustal metamorphic conditions, and can be negative if the entrapment conditions are low pressures close and beyond the α–β quartz transition (Fig. 2). The residual

90 differential stress is uniaxial with the symmetry axis of the stress parallel to the c-axis of the quartz inclusion. Stress on the inclusion is hydrostatic ($\sigma_c - \sigma_a = 0$) for a thermal gradient of ~220 °C/GPa or ~6 °C/km. Stress along the *c*-axis is higher than

along the *a*-axis for higher temperature and lower pressure conditions, and lower for lower temperatures and higher pressures that are uncommon in metamorphic rocks. Residual pressure is more sensitive to entrapment pressure and residual stress to entrapment temperature (Fig. 2). A combined determination of the two has potential geothermobarometric

95 application (Alvaro et al., 2019).

4. Results

4.1. Hydrostatic compression

The hydrostatic pressure effects were calibrated in the range 0-2 GPa that covers applications of piezospectroscopy to metamorphic quartz inclusions (Fig. 3). For the 128 and 464 cm^{-1} peaks, the present results are consistent with previous

100 calibrations (Schmidt and Ziemann, 2000) with a maximum deviation of 0.4 cm^{-1}, and an average deviation of 0.1 cm^{-1}, i.e. within the inferred accuracy of Raman spectroscopy when internal standards provided here by Ne or Hg emission lines are used.

For the sake of comparison with former studies, data were fitted with the expression:

$$P = A\Delta v_h + B\Delta v_h^2 \tag{1},$$

105 where Δv_h is the shift under hydrostatic stress with respect to the ambient conditions wavenumber (v) of the Raman peak. Values of A and B reported in Table 1 for the three main peaks of quartz. The Raman shift and its derivative are:

$$\Delta v_h = [-A + (A^2 + 4BP)^{1/2}]/2B \tag{2},$$

$$(\partial v/\partial P)_0 = (A^2 + 4BP)^{-1/2} \tag{3}.$$

It is worth noting that if the calibration is performed including data at pressures above 2 GPa, the initial slope is

110 underestimated with respect to the present value, especially for the 206 cm^{-1} peak. This is related to the complex pressure dependence of quartz Raman spectrum beyond the 2 GPa pressure range (Morana et al., 2020; Hemley, 1987). The present calibration is particularly adapted for applications to quartz inclusions that are under residual pressures below 2 GPa, a condition that applies even to those that underwent conditions in the stability field of coesite with residual pressure below 1.3 GPa (Alvaro et al., 2019).

115 ### 4.2. Uniaxial compression

The effects of uniaxial stress, applied either parallel or perpendicular-to the c-axis of quartz, differ strongly from peak to peak (Table 1). Stress effects are linear within uncertainties within the investigated range of stress up to ~0.6 GPa beyond which crystals break. For the 206 cm^{-1} peak, the effects of stress are similar within uncertainties along the *a*- and *c*-axis (Fig. 3c), with a stress dependence of 10.0(4) and 10.8(2) cm^{-1}/GPa, respectively. The sum of the axial stress dependence of

120 30.8(10) cm^{-1}/GPa is similar to the bulk pressure induced shift of 30.7(13) cm^{-1}/GPa at ambient pressure. Tekippe et al

(1973) also observed an independence of the 206 cm^{-1} peak shift on the compression direction, with a stress dependence of 7.4(2) cm^{-1}/GPa consistent with the bulk pressure dependence of 21.4 cm^{-1}/GPa. The consistency between the sum of axial stress dependence and hydrostatic pressure experiment confirm that the stress and Raman shift have been accurately measured. Because the shift of the 206 cm^{-1} peak is independent of the stress orientation within uncertainty, its position

125   gives an absolute reading of the pressure P whether the stress is hydrostatic or not.

For the 128 and 464 cm^{-1}, the shift is very different when stress is applied perpendicular or parallel to the c axis. For stress applied along directions perpendicular to c, the TO and LO components of the 128 cm^{-1} mode of E symmetry split due to the piezoelectric effect and symmetry breaking (Tekippe et al., 1973). The TO-LO splitting is characteristic of differential stress in the basal plane of quartz, a property that was used to measure differential stresses in non-hydrostatic experiments with

130   DAC (Reynard et al., 2019). The symmetry breaking for uniaxial compression along the a-axis does not significantly affect the analysis performed later in trigonal symmetry for geological applications (Murri et al., 2022). The shifts of the 128 and 464 cm^{-1} peaks relative to the 206 cm^{-1} peak are linear within the investigated stress range (Fig. 4).

5. Comparison with former studies

5.1. Hydrostatic compression

135   The present variation of the 206 cm^{-1} peak shows an increasing discrepancy with that of Schmidt and Ziemann (2000) with increasing pressure, reaching about 1.5 cm^{-1} at 1.5 GPa (Fig. 3a), above the accuracy of the measurement. This discrepancy is due to the use of a symmetric Voigt function in the present study when Schmidt and Ziemann (2000) used an asymmetric Pearson IV distribution. For piezospectroscopic applications, the Voigt function is widely used to fit the 206 cm^{-1} peak position (Alvaro et al., 2019; Bonazzi et al., 2019; Cisneros et al., 2020; Cisneros et al., 2021; Enami et al., 2007; Gonzalez

140   et al., 2019; Thomas and Spear, 2018; Zhong et al., 2019) because it avoid unrealistic fits due to interference with host mineral Raman peaks (garnet in most cases). Thus the present hydrostatic calibration of the 206 cm^{-1} peak position is appropriate for common practice in quartz-inclusion Raman geobarometry. The pressure difference between the two calibrations is about 2%, it does not affect significantly the pressure estimates but improves the self-consistency in the calculations of residual differential stress on inclusions (see below). Grüneisen plot (Fig. 3b) shows that the assumption of

145   constant Grüneisen parameters (Angel et al., 2019) is not valid in quartz, except for the 464 cm^{-1} peak. Grüneisen parameter (γ) dependence on pressure is taken into account in fitting the data (Table 1) with two parameters (Reynard et al., 2012), the ambient pressure value γ_0, and its pressure dependence q expressed as q=($\partial\ln\gamma/\partial\ln V$).

5.2. Non-hydrostatic compression

The relative shifts of the 128 and 464 cm^{-1} peaks with respect to the 206 cm^{-1} peak are remarkably constant between present

150   experiments at 295 K and those at 4 K (Tekippe et al., 1973). Absolute values of stress-induced shifts are lower at 4 K than

in the present ambient temperature experiment because quartz is stiffer and has a lower volume corresponding to that for a compression at about 0.25 GPa at ambient temperature. Shifts from the first-principles calculations (Murri et al., 2019) are compared to the experimental ones through the Grüneisen parameters listed in Table 1. To derive the Grüneisen tensor components from the present measurements, one needs to convert between stress and strain via the stiffness tensor. The

155   Raman shift is related to stress as follows assuming $\sigma_1 = \sigma_2$ due to symmetry:

$$\Delta \nu = 2 \left(\frac{\partial \nu}{\partial \sigma_1}\right)_{\sigma_3} \sigma_1 + \left(\frac{\partial \nu}{\partial \sigma_3}\right)_{\sigma_1} \sigma_3 \qquad (4),$$

where $\left(\frac{\partial \nu}{\partial \sigma_1}\right)_{\sigma_3}$ and $\left(\frac{\partial \nu}{\partial \sigma_3}\right)_{\sigma_1}$ are directly fitted from experiment (Table 1) and assumed constant. From linear elasticity, we have:

$$\sigma_1 = (C_{11} + C_{12})\varepsilon_1 + C_{13}\varepsilon_3 \qquad (5),$$

160    $$\sigma_3 = 2\, C_{13}\varepsilon_1 + C_{33}\varepsilon_3 \qquad (6),$$

where C_{ij} are the components of the elastic stiffness tensor. The shear components of strain and stress are not present because for symmetry preserved crystal (i.e. $\sigma_1 = \sigma_2$), and the off-diagonal strain components are all zero due to $C_{41} = -C_{42}$. Substituting σ_1 and σ_3 into equation (4), and collecting common terms for ε_1 and ε_3, we have:

$$\Delta \nu = 2 \left[\left(\frac{\partial \nu}{\partial \sigma_1}\right)_{\sigma_3} (C_{11} + C_{12}) + \left(\frac{\partial \nu}{\partial \sigma_3}\right)_{\sigma_1} C_{13}\right] \varepsilon_1 + \left[2 \left(\frac{\partial \nu}{\partial \sigma_1}\right)_{\sigma_3} C_{13} + \left(\frac{\partial \nu}{\partial \sigma_3}\right)_{\sigma_1} C_{33}\right] \varepsilon_3 \qquad (7).$$

165   The Grüneisen tensor components are obtained by dividing the terms in square bracket by the peak position at zero stress ν_0:

$$\gamma_1 = \left[\left(\frac{\partial \nu}{\partial \sigma_1}\right)_{\sigma_3} (C_{11} + C_{12}) + \left(\frac{\partial \nu}{\partial \sigma_3}\right)_{\sigma_1} C_{13}\right]/\nu_0 \qquad (8),$$

$$\gamma_3 = \left[2 \left(\frac{\partial \nu}{\partial \sigma_1}\right)_{\sigma_3} C_{13} + \left(\frac{\partial \nu}{\partial \sigma_3}\right)_{\sigma_1} C_{33}\right]/\nu_0 \qquad (9).$$

Using the values for $\left(\frac{\partial \nu}{\partial \sigma_1}\right)_{\sigma_3}$, $\left(\frac{\partial \nu}{\partial \sigma_3}\right)_{\sigma_1}$ obtained here and published values of C_{ij} (Heyliger et al., 2003), we obtain the values reported in Table 1.

170   Shifts with uniaxial stress from first-principles calculations (Murri et al., 2019) are roughly consistent with experimental values for the 464 cm^{-1} peaks, and divergent for the 128 and 206 cm^{-1} mode. These differences are possibly due to shortcomings of the first-principles calculations such as unaccounted for anharmonic effects and TO-LO splitting, or to assumption of constant Grüneisen parameters used in fitting theoretical results. Constant Grüneisen parameters are inconsistent with the pressure shifts of the 128 and 206 cm^{-1} peaks (Fig 3b). It shows that the discrepancy between theory

175   and experiments, although reasonable given the absence of fitted parameters in the first-principles models, is significant

when trying to apply results to quartz piezobarometry. Thus we reexamine in the following the relationships between Raman peak positions and pressure and differential stress for quartz inclusions with the experimental shifts determined here.

6. Applications to piezospectroscopy of quartz inclusions

A spherical monocrystalline inclusion is subjected to triaxial normal stresses with principal components $\sigma_1, \sigma_2, \sigma_3$. The

180   Raman shift ν is a function of these principal stresses and their orientation with respect to that of the crystal. Here we set σ_3 parallel to the c-axis of the inclusion. For the 206 cm^{-1} peak, the shifts with differential stress are similar along and perpendicular to the c-axis, and the Raman frequency will depend only on the residual pressure P defined as the first invariant of the stress tensor ($P = \frac{\sigma_1+\sigma_2+\sigma_3}{3}$). It is only for the 464 and 128 cm^{-1} peaks that the different stresses will influence the Raman shift in response to both P and the differential stresses. Since TO-LO splitting of the 128 cm^{-1} mode is

185   not observed in Raman measurements on quartz inclusions, it is assumed that there is no significant difference between σ_1 and σ_2.

With a uniaxial differential stress along the major symmetry axis of the quartz inclusion, the stress tensor can be written:

$$\begin{pmatrix} P - 1/3\sigma & 0 & 0 \\ 0 & P - 1/3\sigma & 0 \\ 0 & 0 & P + 2/3\sigma \end{pmatrix} \quad\quad (10),$$

where $\sigma = \sigma_3 - \sigma_1 = \sigma_c - \sigma_a$ is the residual differential stress in the inclusion where a and c refer to the crystallographic

190   axes of quartz. The shift $\Delta\nu_{\text{nh}}$ of a Raman peak of wavenumber ν with the differential stress is:

$$\Delta\nu_{\text{nh}} = \Delta\nu - \Delta\nu_{\text{h}} = 2/3\ \sigma\ \left(\frac{\partial\nu}{\partial\sigma_3}\right)_{\sigma_1} - 2/3\ \sigma\ \left(\frac{\partial\nu}{\partial\sigma_1}\right)_{\sigma_3} \quad\quad (11).$$

where $\Delta\nu_{\text{h}}$ is the hydrostatic shift from equation (2), $\Delta\nu$ is the measured shift with respect to ambient conditions, and $\left(\frac{\partial\nu}{\partial\sigma_i}\right)_{\sigma_j}$ are fitted slopes to the data under uniaxial compression. It is worth noting that while the shifts with pressure required fitting with a quadratic expression, the shifts with stress $\left(\frac{\partial\nu}{\partial\sigma_i}\right)_{\sigma_j}$ are assumed linear (Fig. 3 and 4, Table 1).

195   Combining (11) and (2) and solving for the stress, we obtain:

$$\sigma \approx 3/2\ [\Delta\nu - (- A + (A^2 + 4B \times P_{206})^{1/2})/2B)]/[\ \left(\frac{\partial\nu}{\partial\sigma_3}\right)_{\sigma_1} - \sigma\ \left(\frac{\partial\nu}{\partial\sigma_1}\right)_{\sigma_3}\ ] \quad\quad (12),$$

where P_{206} is the pressure obtained from the position of the 206 cm^{-1} peak, and A and B are the fitted coefficients from the hydrostatic experiment given in Table 1. The non-hydrostatic stress can be obtained from the positions of both the 464 and 128 peaks, and checked for self-consistency. Using the values in Table 1, where for the 128 peak the average slopes for the

200   TO-LO components are used, stresses (in GPa) are obtained:

$$\sigma(464) \approx 1.5 \times [\Delta \nu(464) - (-0.107 + (0.107^2 + 0.0032 \times P_{206})^{1/2})/0.0016)]/(-2.7) \qquad (13),$$

$$\sigma(128) \approx 1.5 \times [\Delta \nu(128) - (-0.127 + (0.127^2 + 0.0204 \times P_{206})^{1/2})/0.0102)]/(1.8) \qquad (14).$$

To summarize, discrepancies between pressures obtained from the three Raman peaks are expected with increasing residual differential stress. The position of the 206 cm^{-1} peak is independent of differential stress σ, and gives the hydrostatic

205   pressure. If the residual differential stress is non-zero, residual pressures obtained from the 128 and 464 cm^{-1} peaks should be shifted with respect to values obtained with the 206 cm^{-1} peak, by amounts of opposite signs. A routine for calculating pressure and stresses from the Raman peak positions is provided in the supplementary Excel spreadsheet.

6.1. Comparison with experimental inclusions

Bonazzi et al. (2019) synthesized quartz inclusions in almandine at 2.5 GPa 800°C and 3 GPa 775°C. The present

210   calibration was tested on their selection of inclusions based on optical criteria (absence of cracks, sufficient distance from garnet rim and other inclusions, ...). For most of these inclusions the residual pressures inferred from the 206 cm^{-1} peak position are consistent with those expected from elastic modeling of quenching and decompression from the experimental equilibration conditions (Fig. 5a).

Several inclusions synthesized at 3 GPa display residual pressures lower than expected and that are inconsistent between the

215   three peaks (Fig. 5b), indicating large differential residual differential stresses (Fig. 5c). For those, the inferred residual differential stresses are of opposite signs when estimated using the 128 or 464 cm^{-1} peaks, with values of σ between ~ -0.5 and 2 GPa using the 464 cm^{-1} peak, and between ~ 0.5 and -3 GPa using the 128 cm^{-1} peak. It indicates these inclusions are under a stress pattern that is not consistent with simple elastic deformation. The large residual differential stresses are likely due to unobserved defects around inclusions.

220   We propose to use the inconsistency in residual differential stress calculated here directly from Raman peak positions and equations (1,13,14) as a guide to eliminate those inclusions under complex stress state from the analysis of residual pressures. Thus we discarded from the analysis inclusions with an absolute difference in residual differential stress from the 128 and 464 cm^{-1} peak positions larger than an arbitrary value of 1 GPa (see supplementary table). This changes the average residual pressure from 1.06(3) to 1.11(3) GPa. Both residual pressure averages are within uncertainties of the value of 1.08

225   GPa expected from the elastic model. The average value of residual differential stresses after selection of 0.00(10) and $-0.03(11)$ is close to that of 0.0 GPa expected from elastic modeling (Fig. 2), when the one prior to selection is $\sim -0.5(2)$ and 0.4(2) GPa for the 128 and 464 cm^{-1} peaks, respectively. Bonazzi et al. (2019) proposed a correction for similar effects in strains using the first-principles strain-induced shifts (Murri et al., 2019), which are discrepant with the present experimental stress-induced shifts (Table 1). The assumed relationship between strain and stress underlying the correction is not provided,

230   preventing direct comparison with the present results.

The inclusions synthesized at 2.5 GPa yield residual pressures of 0.82(1) after selection with the above-defined criterion from both the 206 and 464 cm^{-1} peaks (Fig. 5b, supplementary table). They are consistent with those of the elastic model of

0.86 GPa. Residual pressures from the 128 cm^{-1} peak are systematically lower by ~0.1 GPa. As a result, residual differential stress is −0.01(4) for the 464 cm^{-1} peak, and of ~ −0.4(1) for the 128 cm^{-1} peak, where a value of −0.05 GPa is expected

235   from the elastic model at 2.5 GPa and 800°C (Fig. 2). The systematic shift of residual stress values from the 1:1 line (Fig. 5c) is possibly due to systematic uncertainties in the Raman peak positions for this particular set of inclusions.

6.2. Comparison with natural inclusions

We used recent datasets on natural inclusions from three different metamorphic suites: 1) blueschists from Syros in garnet formed at ~1.4–1.7 GPa and 500–550 °C, and in retrograde epidote grown between ~1.3–1.5 GPa 400–500 °C and ~1.0 GPa

240   and 400 °C (Cisneros et al., 2021); 2) Holsnøy eclogite from the Bergen Arcs (Norway) where inclusions formed at 1.4–1.6 GPa, 680–760 °C consistent with previous estimates based on phase equilibria (Zhong et al., 2019; Bhowany et al., 2018); 3) gneiss from Papua New Guinea with formation conditions estimated from Ti in quartz and quartz in garnet inclusions as ~1.0 GPa and 600 °C, which are interpreted as the P–T conditions of garnet growth and entrapment of quartz inclusions (Gonzalez et al., 2019).

245   The residual pressures estimated from the present calibration are within uncertainties of those published using earlier calibrations. The major difference comes from the possibility of estimating here the residual differential differential and to use it as a criterion for validating measurements (section 6.1). Residual pressures from the 128 and 464 cm^{-1} peaks are respectively higher and lower than hydrostatic pressure from the 206 cm^{-1} peak in rocks from Papua-New Guinea, indicating significant residual differential stress. They are almost indistinguishable within uncertainties for blueschists of Syros,

250   indicating little residual differential stress (Fig. 6a).

Residual differential stresses σ_{128} and σ_{464} are self-consistent and low, with average values of less than 0.3 GPa (Fig. 6b, supplementary table). Average values are well defined except in inclusions from Norway where the 128 cm^{-1} peak position is imprecise due to spectrometer configuration, and because of the small number of measurable inclusions. The dispersion of individual values is accounted for by uncertainties in Raman peak position (Fig. 6b). The smaller dispersion of residual

255   differential stresses in natural inclusions than in experimental ones likely reflect longer natural relaxation timescales versus fast quenching and pressure release in experiments. With the method and calibration proposed here, all but five measured natural inclusions (see supplementary table) fall within the conditions defined for the calibration of uniaxial differential stress along the major symmetry axis of the quartz inclusion at the beginning of section 6. In the opposite, the method using strain anisotropy resulted in the rejection of 74 inclusions out of 92 (Gonzalez et al., 2019). This high rejection rate stems

260   from the discrepancies between Grüneisen parameters (Murri et al., 2019) used to calculate strains (Angel et al., 2019) and those experimentally determined in the present study (Table 1).

Average values of residual differential stress from both the 128 and 464 cm^{-1} peaks are −0.04(4) GPa, −0.18(3) GPa, and −0.16(14) GPa for Syros, Papua-New Guinea, and Norway, respectively, with a similar trend to values expected from the elastic model, of −0.06(3), −0.13(3) and −0.14(4), respectively (Fig. 2). Taken at face values, residual differential stresses in

265 Syros and Papua-New Guinea translate into temperatures of 340-600 and 640-830°C, respectively, to be compared with 500-550 and 600°C estimated from independent phase equilibria and geothermometers (Cisneros et al., 2021; Gonzalez et al., 2019). For the Holsnøy eclogite (Norway), the mean value of residual stress yields ~750°C within the range of 680-760°C from previous estimates (Zhong et al., 2019), although the temperature range is not precisely defined owing to the large uncertainty on residual stress. It suggests that independent constrain on temperature of entrapment may be obtained from

270 residual differential stresses on inclusions. This would require reducing uncertainties by measuring residual pressures and differential stresses on a large number of inclusions, by systematic calibration of Raman measurements with He or Hg emission lines (section 2), and calibration on samples formed in well-characterized metamorphic conditions. The effect of large numbers of analyses on improving the accuracy of residual stress measurements is clearly seen when comparing mean values and uncertainties (Fig. 6b) from small (Norway, 11 inclusions), medium (Syros, 22) and large (Papua-New Guinea,

275 92) datasets.

7. Concluding remarks

The present calibration can be used to directly estimate the residual pressures and differential stresses using simple relationships established between Raman shifts, pressure and uniaxial stresses. Hydrostatic pressure is obtained from the 206 cm^{-1} peak position that is insensitive to residual stress. Self-consistency of residual differential stresses obtained from the

280 128 cm^{-1} and 464 cm^{-1} peak positions is an objective filter to detect inclusions that are under stress conditions where assumptions used for elastic modeling of entrapment conditions do not apply. Residual stress effects on the pressures determined with 128 cm^{-1} and 464 cm^{-1} peaks are of similar magnitude and opposite sign, hence the average of these two values is a good estimate of the hydrostatic pressure if the 206 cm^{-1} peak cannot be measured accurately due to interference with host mineral peaks. Using the 128 and 464 cm^{-1} peak alone, or averaging either 128 and 206 or 206 and 464 cm^{-1} peaks

285 can induce systematic bias in the residual pressure determination.

Residual differential stresses observed in suites of metamorphic rock inclusions suggest they depend on temperature at the time of entrapment. Reduction of uncertainties and calibration on rocks with various conditions of formation would be necessary for use as a quantitative geothermometer. Large numbers of inclusions should be measured and uncertainties on Raman data reduced with the systematic use of internal calibration lines. Reduction of uncertainties may also require Raman

290 measurements at combined high pressure and high stress, currently an experimental challenge, and elastic constant determinations at combined high pressure and temperature to limit extrapolation in elastic model predictions.

Competing interests. The authors have no competing financial interests or personal relationships that could have influenced the work shown in this publication.

295

Acknowledgments. This work was supported by grants to BR through LABEX Lyon Institute of Origins (ANR-10-LABX-0066) of the Université de Lyon within the Plan France 2030 of the French government operated by the National Research Agency (ANR).

300 **References**

Alvaro, M., Mazzucchelli, M. L., Angel, R. J., Murri, M., Campomenosi, N., Scambelluri, M., Nestola, F., Korsakov, A., Tomilenko, A. A., Marone, F., and Morana, M.: Fossil subduction recorded by quartz from the coesite stability field, Geology, 48, 24-28, 10.1130/G46617.1, 2019.

Angel, R. J., Allan, D. R., Miletich, R., and Finger, L. W.: The Use of Quartz as an Internal Pressure Standard in High-Pressure

305 Crystallography, Journal of Applied Crystallography, 30, 461-466, https://doi.org/10.1107/S0021889897000861, 1997.

Angel, R. J., Alvaro, M., Miletich, R., and Nestola, F.: A simple and generalised P–T–V EoS for continuous phase transitions, implemented in EosFit and applied to quartz, Contributions to Mineralogy and Petrology, 172, 29, 10.1007/s00410-017-1349-x, 2017a.

Angel, R. J., Mazzucchelli, M. L., Alvaro, M., and Nestola, F.: EosFit-Pinc: A simple GUI for host-inclusion elastic thermobarometry, American Mineralogist, 102, 1957-1960, doi:10.2138/am-2017-6190, 2017b.

310 Angel, R. J., Murri, M., Mihailova, B., and Alvaro, M.: Stress, strain and Raman shifts, 234, 129-140, doi:10.1515/zkri-2018-2112, 2019.

Bhowany, K., Hand, M., Clark, C., Kelsey, D. E., Reddy, S. M., Pearce, M. A., Tucker, N. M., and Morrissey, L. J.: Phase equilibria modelling constraints on P–T conditions during fluid catalysed conversion of granulite to eclogite in the Bergen Arcs, Norway, Journal of Metamorphic Geology, 36, 315-342, https://doi.org/10.1111/jmg.12294, 2018.

Bonazzi, M., Tumiati, S., Thomas, J. B., Angel, R. J., and Alvaro, M.: Assessment of the reliability of elastic geobarometry with quartz

315 inclusions, Lithos, 350-351, 105201, https://doi.org/10.1016/j.lithos.2019.105201, 2019.

Briggs, R. J. and Ramdas, A. K.: Piezospectroscopy of Raman spectrum of alpha-quartz, Physical Review B, 16, 3815-3826, 10.1103/PhysRevB.16.3815, 1977.

Carpenter, M. A., Salje, E. K. H., Graeme-Barber, A., Wruck, B., Dove, M. T., and Knight, K. S.: Calibration of excess thermodynamic properties and elastic constant variations associated with the alpha <-->beta phase transition in quartz, American Mineralogist, 83, 2-

320 22, 10.2138/am-1998-1-201, 1998.

Cisneros, M., Ashley, K. T., and Bodnar, R. J.: Evaluation and application of the quartz-inclusions-in-epidote mineral barometer, American Mineralogist, 105, 1140-1151, 10.2138/am-2020-7379, 2020.

Cisneros, M., Barnes, J. D., Behr, W. M., Kotowski, A. J., Stockli, D. F., and Soukis, K.: Insights from elastic thermobarometry into exhumation of high-pressure metamorphic rocks from Syros, Greece, Solid Earth, 12, 1335-1355, 10.5194/se-12-1335-2021, 2021.

325 Connolly, J. A. D.: Multivariable phase diagrams; an algorithm based on generalized thermodynamics, American Journal of Science, 290, 666--718, 10.2475/ajs.290.6.666, 1990.

Enami, M., Nishiyama, T., and Mouri, T.: Laser Raman microspectrometry of metamorphic quartz: A simple method for comparison of metamorphic pressures, American Mineralogist, 92, 1303-1315, 10.2138/am.2007.2438, 2007.

Gonzalez, J. P., Thomas, J. B., Baldwin, S. L., and Alvaro, M.: Quartz-in-garnet and Ti-in-quartz thermobarometry: Methodology and first

330 application to a quartzofeldspathic gneiss from eastern Papua New Guinea, Journal of Metamorphic Geology, 37, 1193-1208, https://doi.org/10.1111/jmg.12508, 2019.

Hemley, R. J.: Pressure dependence of Raman spectra of SiO_2 polymorphs: a quartz, coesite and stishovite, in: High-pressure research in mineral physics., edited by: Manghnani, M. H., and Syono, Y., Terra Scientific, Tokyo, 347-360, 1987.

Heyliger, P. R., Ledbetter, H. M., and Kim, S. A.: Elastic Constants of Natural Quartz, Journal of the Acoustical Society of America, 114,

335 644-650, 10.1121/1.1593063, 2003.

Holland, T. J. B. and Powell, R.: An internally consistent thermodynamic data set for phases of petrological interest, Journal of metamorphic Geology, 16, 309-343, 10.1111/j.1525-1314.1998.00140.x, 1998.

Izreali, E. S., Harris, J. W., and Navon, O.: Raman barometry of diamond formation, Earth and Planetary Science Letters, 173, 351-360, 1999.

340 Kohn, M. J.: "Thermoba-Raman-try": Calibration of spectroscopic barometers and thermometers for mineral inclusions, Earth and Planetary Science Letters, 388, 187-196, https://doi.org/10.1016/j.epsl.2013.11.054, 2014.

Morana, M., Mihailova, B., Angel, R. J., and Alvaro, M.: Quartz metastability at high pressure: what new can we learn from polarized Raman spectroscopy?, Physics and Chemistry of Minerals, 47, 34, 10.1007/s00269-020-01100-y, 2020.

Murri, M., Alvaro, M., Angel, R. J., Prencipe, M., and Mihailova, B. D.: The effects of non-hydrostatic stress on the structure and

345 properties of alpha-quartz, Physics and Chemistry of Minerals, 46, 487-499, 10.1007/s00269-018-01018-6, 2019.

Murri, M., Gonzalez, J. P., Mazzucchelli, M. L., Prencipe, M., Mihailova, B., Angel, R. J., and Alvaro, M.: The role of symmetry-breaking strains on quartz inclusions in anisotropic hosts: Implications for Raman elastic geobarometry, Lithos, 422-423, 106716, https://doi.org/10.1016/j.lithos.2022.106716, 2022.

350   Parkinson, C. D. and Katayama, I.: Present-day ultrahigh-pressure conditions of coesite inclusions in zircon and garnet: Evidence from laser Raman microspectroscopy, Geology, 27, 979-982, 10.1130/0091-7613(1999)027<0979:pdupco>2.3.co;2, 1999.

Piermarini, G. J., Block, S., Barnett, J. D., and Forman, R. A.: Calibration of the pressure dependence of the R1 ruby fluorescence line to 195 kbar, Journal of Applied Physics, 46, 2774-2780, 10.1063/1.321957, 1975.

Reynard, B., Bezacier, L., and Caracas, R.: Serpentines, talc, chlorites, and their high-pressure phase transitions: a Raman spectroscopic study, Physics and Chemistry of Minerals, 1-9, 10.1007/s00269-015-0750-0, 2015.

355   Reynard, B., Montagnac, G., and Cardon, H.: Raman spectroscopy at high pressure and temperature for the study of the Earth's mantle and planetary materials, in: EMU Notes in Mineralogy, Vol. 12, edited by: Dubessy, J., Caumon, M., and Rull, F., 12, 365-388, 10.1180/EMU-notes.12.10, 2012.

Reynard, B., Caracas, R., Cardon, H., Montagnac, G., and Merkel, S.: High-pressure yield strength of rocksalt structures using quartz Raman piezometry, Comptes Rendus Geoscience, 351, 71-79, https://doi.org/10.1016/j.crte.2018.02.001, 2019.

360   Schmidt, C. and Ziemann, M. A.: In-situ Raman spectroscopy of quartz: A pressure sensor for hydrothermal diamond-anvil cell experiments at elevated temperatures, American Mineralogist, 85, 1725-1734, 10.2138/am-2000-11-1216, 2000.

Tekippe, V. J., Ramdas, A. K., and Rodrigue.S: Piezospectroscopic study of Raman-spectrum of alpha-quartz, Physical Review B, 8, 706-717, 10.1103/PhysRevB.8.706, 1973.

Thomas, J. B. and Spear, F. S.: Experimental study of quartz inclusions in garnet at pressures up to 3.0 GPa: evaluating validity of the
365   quartz-in-garnet inclusion elastic thermobarometer, Contributions to Mineralogy and Petrology, 173, 42, 10.1007/s00410-018-1469-y, 2018.

Zhong, X., Dabrowski, M., and Jamtveit, B.: Analytical solution for residual stress and strain preserved in anisotropic inclusion entrapped in an isotropic host, Solid Earth, 12, 817-833, 10.5194/se-12-817-2021, 2021.

Zhong, X., Andersen, N. H., Dabrowski, M., and Jamtveit, B.: Zircon and quartz inclusions in garnet used for complementary Raman
370   thermobarometry: application to the Holsnøy eclogite, Bergen Arcs, Western Norway, Contributions to Mineralogy and Petrology, 174, 50, 10.1007/s00410-019-1584-4, 2019.
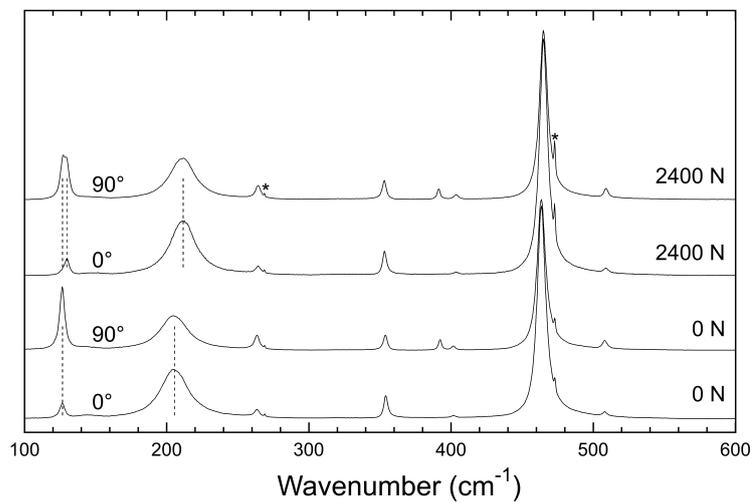
375

Figure 1. Typical spectra of quartz at ambient conditions (0 N) and under uniaxial force of 2400 N corresponding to a stress of ~0.6 GPa) along the *a*-axis. Spectra were measured with two perpendicular polarizer orientations to better characterize the TO-LO splitting of the 128 cm^{-1} E mode under stress. Asterisks mark the calibration Ne and Hg lines near 269.5 and 473.5 cm^{-1}.

380
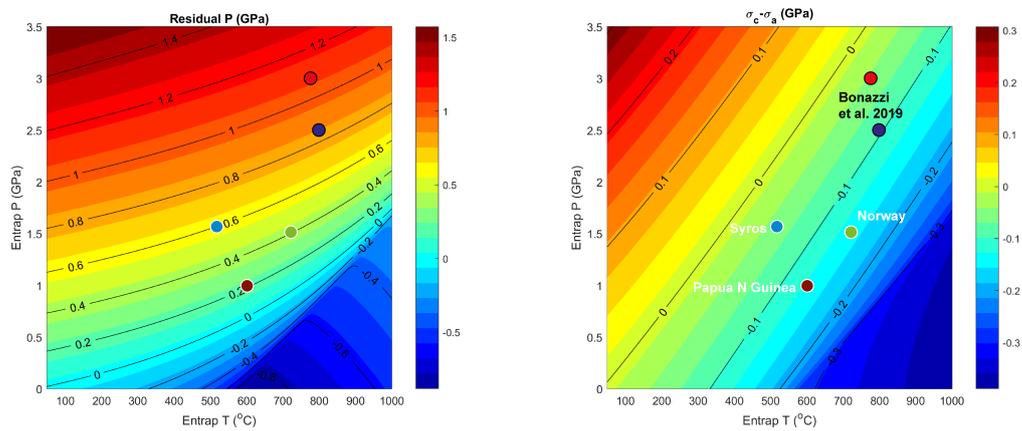
Figure 2. Model residual pressure and residual differential stress on quartz included in almandine. Expected residual
pressure and stress corresponding to conditions of entrapment of experimental and natural inclusions are shown for
comparison with measured values (Figs. 5 and 6). Actual pressures for natural inclusions may be shifted by less than 0.05
GPa due to compositional effects on garnet equation of state.
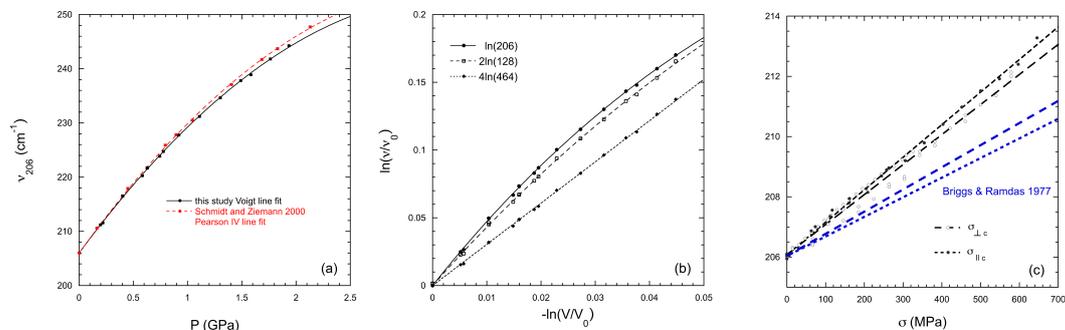
390

Figure 3. (a) Dependence of the 206 cm^{-1} peak on hydrostatic pressure at ambient temperature. The small discrepancy between present hydrostatic compression data and former experimental data (Schmidt and Ziemann, 2000) is due to fitting with different peak shape (symmetrical Voigt used here instead of asymmetrical Pearson IV). (b) Grüneisen plot showing constant Grüneisen parameter for the 464 cm^{-1} peak and strong curvature for other peaks. Relative frequency shifts are

395 multiplied by 2 and 4 for the 128 and 464 cm^{-1} peaks, respectively, for the sake of easy comparison. (c) Dependence on uniaxial stress obtained here are higher than those measured at 4 K (Briggs and Ramdas, 1977; Tekippe et al., 1973), due to temperature effects. The variations in peak position depends little on compression direction for the 206 cm^{-1} peak in both studies, indicating its position depends essentially on hydrostatic pressure.

400
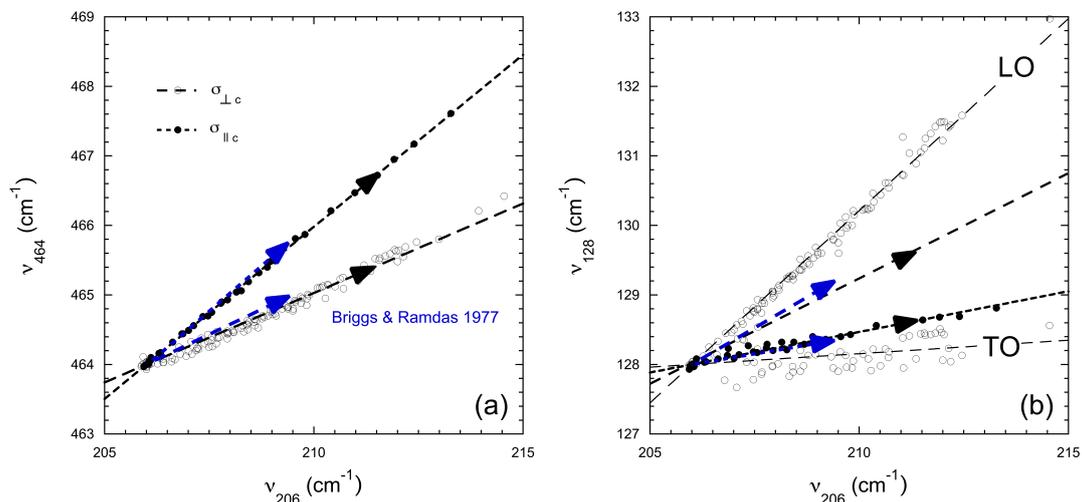
Figure 4. Stress dependence of the (a) 464 and (b) 128 cm^{-1} peaks relative to the 206 cm^{-1} peak at ambient temperature. Arrows show the shift for a uniaxial stress of 0.5 GPa from experiments at ambient conditions (this study), and at 4 K

405 (Briggs and Ramdas, 1977; Tekippe et al., 1973). For the 128 cm^{-1} peak, the transverse (TO) and longitudinal (LO) optic modes are split by compression perpendicular to the c-axis, with the LO component at higher frequency than the TO component. Stress dependence (long-dashed line) is the average of that of the TO and LO components (Tekippe et al., 1973). A few data points were collected at effective stresses higher than 0.6 GPa in partially broken crystals. The stress is then not calibrated because the crystal section is not known anymore, these points plot along extrapolation of the linear trends even

410 though they were not included in the fit.
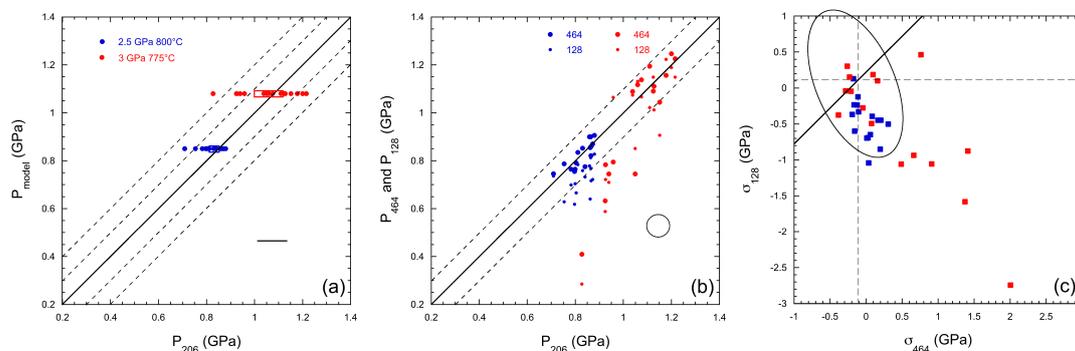
Figure 5. Pressures and stresses obtained from experimental quartz inclusions (Bonazzi et al., 2019). (a) Residual pressures

415   from thermoelastic modeling (Fig. 2) as a function of pressures from the 206 cm^{-1} peak for selected inclusions at the indicated conditions of formation. Empty rectangles show the mean value interval at 95% confidence level (2 standard error). Solid 1:1 line, dashed lines with 0.1 GPa offset are shown. Horizontal bar shows the uncertainty associated with 1 cm^{-1} uncertainty on the 206 cm^{-1} peak position. (b) Pressures from the 128 and 464 cm^{-1} peaks as a function of pressure from the 206 cm^{-1} peak. Residual pressures are in general agreement except for a group of experimental inclusions that show

420   significant departure from the 1:1 line. Ellipse shows the uncertainties associated and 0.5 cm^{-1} uncertainties on the 128-464 cm^{-1} peak positions. (c) Residual differential stresses from the 128 and 464 cm^{-1} peaks are consistent within uncertainties except for the group of inclusions departing from the 1:1 line by more than 1 GPa (see text). Ellipse show the uncertainties associated with 1 and 0.5 cm^{-1} uncertainties on the 206 and 128-464 cm^{-1} peak positions, respectively. Anti-correlated uncertainties are associated with the 1 cm^{-1} uncertainty on the 206 cm^{-1} peak position.

425
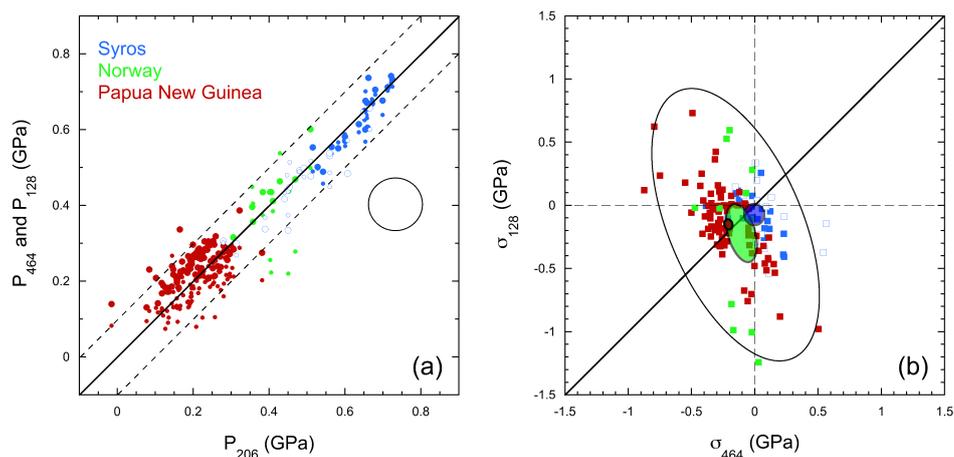
Figure 6. Stresses obtained from natural quartz inclusions. (a) Pressures from the 128 and 464 cm^{-1} peaks (small and large
430 symbols, respectively) deviate from pressure from the 206 cm^{-1} peak with roughly opposite effects of similar magnitude in
Papua and Norway rocks, and differences are negligible in Syros blueschist. (b) Residual differential stresses from the 128
and 464 cm^{-1} peaks. Mean values and confidence interval at 95 % are shown as colored ellipses. Dispersion of individual
measurements are accounted for by systematic uncertainties on Raman measurements (black empty ellipse, same as in Fig.
5c). Residual stresses are negative in Papua-New Guinea and Norway rocks and close to zero in Syros blueschists. Data from
435 Cisneros et al. (2021) for inclusions in garnet (filled symbols) and epidote (empty symbols) in blueschists from Syros
(Cyclade islands, Greece), Gonzalez et al. (2019) for rocks from Papua-New Guinea, Zhong et al. (2019) for eclogitic
inclusions from the Bergen Arcs (Norway). Eleven eclogitic inclusions from Norway were re-measured for this study with
systematic comparison to reference spectrum. Large uncertainties on the 128 cm^{-1} peak position on this dataset are
associated with the high cutoff of the notch filter of the spectrometer in Berlin.

440

Table 1. Pressure and uniaxial stress dependence of the three major Raman peaks of quartz.

	A	B	$\left(\frac{\partial\nu}{\partial P}\right)_0$	γ_0	q	$\left(\frac{\partial\nu}{\partial\sigma_1}\right)_{\sigma_3}$	$\left(\frac{\partial\nu}{\partial\sigma_3}\right)_{\sigma_1}$	γ_1	γ_3	γ_1	γ_3
	GPa/cm^{-1}	GPa/cm^{-2}	cm^{-1}/GPa			cm^{-1}/GPa	cm^{-1}/GPa			[§]	[§]
128(TO)	0.127(6)	0.0051(5)	7.9(4)	2.26(4)	4.7(5)	0.4(3)	1.2(1)	0.11	0.99	*1.21*	*2.69*
128(LO)	0.127(6)	0.0051(5)	7.9(4)	2.26(4)	4.7(5)	5.5(3)	1.2(1)	4.14	2.02	*1.21*[*]	*2.69*[*]
206	0.0326(14)	0.00046(4)	30.7(13)	5.04(6)	6.4(3)	10.0(4)	10.8(2)	5.18	6.71	*3.64*	*5.25*
464	0.107(3)	0.0008(2)	9.4(3)	0.76(0)	-[#]	2.6(2)	5.3(1)	0.66	1.34	*0.60*	*1.19*

[§] First-principles results from Murri et al. (2019) are shown in italics; [*] the TO-LO splitting was not modeled in those calculations; [#] q is not fitted for the 464 cm^{-1} peak.